

Giant Isotope Effect of Thermal Conductivity in Silicon Nanowires

Penghong Ci^{1,2,3}, Muhua Sun⁴, Meenakshi Upadhyaya⁵, Houfu Song⁶, Lei Jin¹, Bo Sun^{6,7},
Matthew R. Jones⁴, Joel W. Ager^{1,2}, Zlatan Aksamija^{5,*} and Junqiao Wu^{1,2,†}

¹*Department of Materials Science and Engineering, University of California, Berkeley, California 94720, USA*

²*Materials Sciences Division, Lawrence Berkeley National Laboratory, Berkeley, California 94720, USA*


³*Institute for Advanced Study, Shenzhen University, Shenzhen 518060, China*

⁴*Department of Chemistry, Rice University, Houston, Texas 77005, USA*

⁵*Department of Electrical and Computer Engineering, University of Massachusetts-Amherst, Amherst, Massachusetts 01003, USA*

⁶*Tsinghua-Berkeley Shenzhen Institute (TBSI), Tsinghua University, Shenzhen 518055, China*

⁷*Tsinghua Shenzhen International Graduate School and Guangdong Provincial Key Laboratory of Thermal Management Engineering and Materials, Shenzhen 518055, China*

 (Received 3 June 2021; revised 11 November 2021; accepted 31 January 2022; published 23 February 2022)

Isotopically purified semiconductors potentially dissipate heat better than their natural, isotopically mixed counterparts as they have higher thermal conductivity (κ). But the benefit is low for Si at room temperature, amounting to only $\sim 10\%$ higher κ for bulk ^{28}Si than for bulk natural Si ($^{\text{nat}}\text{Si}$). We show that in stark contrast to this bulk behavior, ^{28}Si (99.92% enriched) nanowires have up to 150% higher κ than $^{\text{nat}}\text{Si}$ nanowires with similar diameters and surface morphology. Using a first-principles phonon dispersion model, this giant isotope effect is attributed to a mutual enhancement of isotope scattering and surface scattering of phonons in $^{\text{nat}}\text{Si}$ nanowires, correlated via transmission of phonons to the native amorphous SiO_2 shell. The Letter discovers the strongest isotope effect of κ at room temperature among all materials reported to date and inspires potential applications of isotopically enriched semiconductors in microelectronics.

DOI: [10.1103/PhysRevLett.128.085901](https://doi.org/10.1103/PhysRevLett.128.085901)

Thermal management is one of the major bottlenecks to continued scaling of modern microelectronics beyond the current generation, as devices in integrated circuits become increasingly smaller, denser, and more power hungry [1,2]. It is desired to have the active channel of these micro-devices made of semiconductors that not only perform the electronic functions needed, but also quickly dissipate heat away. For silicon, this requirement presents a critical challenge. Although bulk, crystalline Si has a relatively high thermal conductivity ($\kappa \sim 144$ W/mK at room temperature), when its size is reduced to the submicron range, κ is strongly suppressed owing to significant boundary scattering of phonons [3,4]. The reduction in κ becomes even more severe when the surface of the size-reduced Si is rough [5–7], noting that surface or interface roughness exists ubiquitously to a certain degree, especially in nano-structures fabricated via top-down approaches involving chemical etching. It has been reported that, for example, for Si nanowires (NWs) with surface roughness of ~ 3 nm, κ is reduced to the level of ~ 5 W/mK when the diameter is below 100 nm [5,6]. This κ suppression becomes a critical problem for heat dissipation in field effect transistors (FETs) lithographically fabricated from Si wafers, such as fin field effect transistors (FinFETs), [8] and gate-all-around FETs [9]. Alternative materials with high κ near room temperature have been recently investigated as heat dissipation materials for microelectronics, such as boron

phosphide (BP, ~ 490 W/mK) [10], cubic boron nitride (cBN, ~ 880 W/mK) [11], and boron arsenide (BAs, ~ 1000 W/mK) [11–13]. Yet it would be much more impactful if κ of nanoscale Si itself, the channel material of most microelectronic devices, can be drastically improved.

It had been hoped that isotope enrichment of semiconductors would raise κ , as mass disorder arising from isotopes (typically at a few percent or higher atomic fractions) are efficient scatterers to heat-carrying phonons [1,14–16]. The isotope effect of κ is described by the ratio $P = (\kappa_{\text{iso}}/\kappa_{\text{nat}} - 1)$, where κ_{iso} and κ_{nat} are the thermal conductivity of isotopically enriched material and the same material with natural isotope abundances, respectively. A high isotope factor P can arise from strong phonon scattering with isotopes, or conversely a weak umklapp scattering of phonons [1,15,16]. The former is favored by high isotope mass fluctuations [15]. The latter can be weak in the presence of acoustic phonon bunching combined with a wide band gap between acoustic and optical phonons [1,16]. Bulk silicon, unfortunately, meets none of these conditions, resulting in a weak isotope effect of $P \approx 10\%$ at room temperature [17,18].

It has been reported that the isotope effect of κ becomes large in some low-dimensional materials. For example, κ was reported to be enhanced by $\sim 50\%$ in isotopically enriched BN nanotubes at room temperature [19]. An even stronger isotope effect was recently discovered in cubic BN

crystals ($P \sim 108\%$) [20]. A strong isotope effect in κ was also revealed in two dimensional materials, including graphene ($\sim 50\%$) [21], monolayer MoS₂ ($\sim 50\%$) [22], and monolayer BN ($\sim 40\%$) [23,24]. For nanoscale Si, previous studies have reported that isotopically enriched ²⁹Si (99.9%) NWs grown by gold-catalyzed vapor phase epitaxy show $\sim 30\%$ greater κ than ²⁸Si_{0.5}³⁰Si_{0.5} NWs, measured using Raman nanothermometry [25,26]. It is both intriguing and important to ask whether nanoscale Si prepared with top-down methods with naturally rough surfaces [9] would display a stronger isotope effect than bulk Si when isotope scattering, boundary scattering, and umklapp scattering of phonons all interplay and compete. The answer is not straightforward, as a first-order theory would expect the isotope scattering to be further overshadowed by the newly added boundary scattering, leading to P values even lower than in the bulk.

In this Letter, we prepared isotopically enriched ²⁸Si NWs as well as natural Si (^{nat}Si) NWs with sub-100 nm diameters, and directly measured their thermal conductivity. We found that the isotope effect of κ is much enhanced from $\sim 10\%$ in the bulk to 150% in the NWs. Using a model based on a combination of first-principles phonon dispersion and the phonon Boltzmann transport equation, we explain the effect with a two-way coupling between the two distinct phonon scattering mechanisms by mass disorder and by surface roughness. The rates of the two scattering mechanisms are mutually amplified in ^{nat}Si NWs, resulting in the unusually strong isotope effect in κ when the effect is eliminated in ²⁸Si NWs.

Si enriched in the isotope ²⁸Si in the form of SiF₄ was converted to bulk polycrystalline Si by a laboratory-scale reactor, and dislocation-free single crystals (Supplemental Material [27]) were produced from the polycrystalline Si by the float-zone technique [35]. The isotopic composition of the single crystals was measured using secondary ion mass spectroscopy (SIMS) to be 99.920% ²⁸Si, 0.075% ²⁹Si, and 0.005% ³⁰Si; this contrasts with the composition of ^{nat}Si: 92.23% ²⁸Si, 4.67% ²⁹Si, and 3.10% ³⁰Si. These ²⁸Si-enriched crystals (thereafter referred to as ²⁸Si) show a resistivity of approximately 10 Ω cm at room temperature with n -type conduction and free carrier concentration of 3×10^{14} cm⁻³, as reported in previous publications [35]. The concentration of impurities was determined by SIMS to be below 10^{16} cm⁻³ with carbon being the most prominent impurity. The ²⁸Si bulk crystal was then made into NWs using an electroless etching (EE) method in an aqueous solution of AgNO₃ and HF acid [5]. As a reference, ^{nat}Si NWs were also prepared using the same recipe from an n -type ^{nat}Si crystal with very similar resistivity (~ 10 Ω cm). The obtained Si NWs were individually dry transferred to a suspended pad microdevice using a sharp probe for measurement of thermal conductivity [55]. As shown in Fig. 1(a), such a microdevice consists of two suspended pads bridged by the NW to be

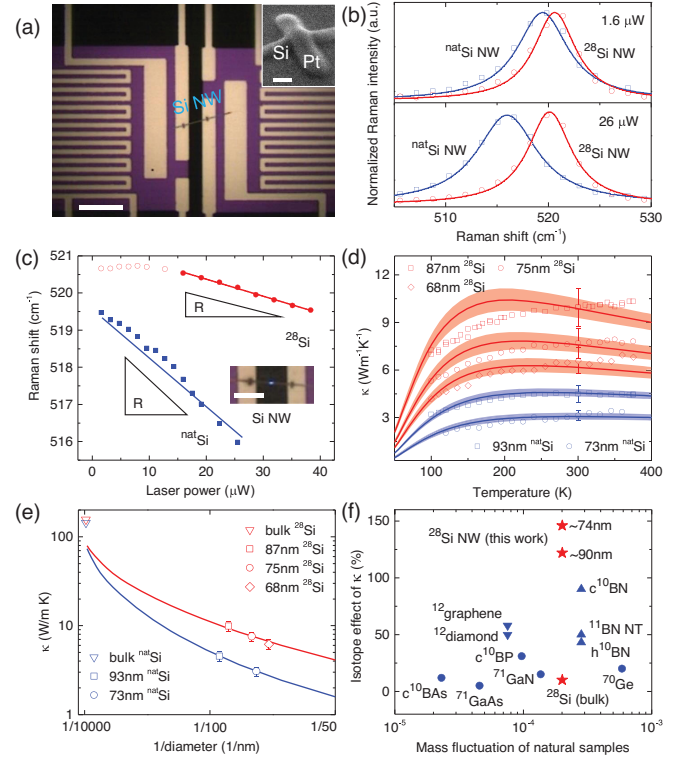


FIG. 1. Thermal conductivity of isotopically enriched (²⁸Si at 99.92%) and natural Si NWs. (a) Optical image of a microdevice consisting of two suspended pads bridged by a Si NW. Inset: SEM image showing the Si NW FIB-bonded by Pt onto the underlying electrodes on the suspended pads. Scale bars: 10 μ m (main panel); 100 nm (Inset). (b) Normalized Raman spectra of suspended Si NWs at a low and a high laser power. (c) Raman peak position as a function of the laser power. Inset: optical image of a suspended NW, where the blue spot shows the focus of the laser beam. Scale bar: 5 μ m. (d) Temperature-dependent thermal conductivity of Si NWs. Symbols are experimental data; curves with shaded thickness are theoretical predictions with 3 nm roughness and 6.5 ± 0.1 (5.1 ± 0.1) nm correlation length for the isotopically enriched (natural) Si NWs. (e) Calculated (curves) and measured (points) thermal conductivity of Si NWs as a function of reciprocal diameter at 300K. (f) Comparison of room-temperature isotope effect of κ of Si NWs compared with that of other isotopically enriched materials reported in the literature. Mass fluctuation parameter of elemental material (A) and compound (AB) is defined as $g_A = \sum_i c_i (1 - M_i/M_{av})^2$ and $g = [(g_A M_A^2 + g_B M_B^2)/(M_A + M_B)^2]$, respectively, where c_i is the atomic fraction of the i th isotope.

measured [5,55,56]. Each pad has a Pt microheater and thermometer to control and sense the temperature, so thermal conductance of the NW can be measured by heat transported from the heating pad to the sensing pad [5,55].

Before accurately measuring the thermal conductivity, Raman spectra were taken from the Si NWs by focusing the laser at the middle of the suspended NWs [inset of Fig. 1(c)]. The Raman spectrum of ²⁸Si NW shows a blueshift with respect to that of ^{nat}Si NW with similar

diameter [Fig. 1(b)], which is expected from the lighter mean atomic mass of ^{28}Si and consistent with results in bulk crystals (Supplemental Material [27]) [57,58]. When the laser power increases, the Raman peak of both NWs redshifts. This is expected as higher laser power heats more the suspended NW at the laser spot, resulting in a redshift of the NW's Raman peak. Interestingly, the $^{\text{nat}}\text{Si}$ NW shows a much stronger redshift than the ^{28}Si NW at the same, increased laser power, which suggests more heat accumulation at the laser spot [59], attributed to a much lower κ of the $^{\text{nat}}\text{Si}$ NW. From the rates of the redshift, it can be estimated that κ of the ^{28}Si NW is approximately two times higher than that of the $^{\text{nat}}\text{Si}$ NW [see Fig. 1(c) and Supplemental Material [27]].

Using the heating and sensing micropads, κ of ^{28}Si and $^{\text{nat}}\text{Si}$ NWs with various diameters were directly measured over a range of temperatures, as shown in Fig. 1(d). The κ values of $^{\text{nat}}\text{Si}$ NWs are in good agreement with what has been reported in literature for synthesis with the EE method [5].

More strikingly, an unusually high isotope effect is observed in these NWs. The Si NWs show an isotope effect ($\kappa_{\text{iso}}/\kappa_{\text{nat}} - 1$) of $\sim 120\%$ and $\sim 150\%$ for NWs with diameter of ~ 90 nm and ~ 74 nm, respectively [Fig. 1(e)]. We also measured κ of bulk crystals of ^{28}Si and $^{\text{nat}}\text{Si}$ using time domain thermoreflectance (TDTR) and found $\kappa_{\text{iso}}/\kappa_{\text{nat}} - 1$ to be only $\sim 10\%$ (Supplemental Material [27]). This low isotope effect in bulk Si is consistent with previous studies [17,18], and is understandable because at room temperature isotope scattering of phonons in $^{\text{nat}}\text{Si}$ would be overshadowed by the much stronger umklapp phonon scattering. The observed isotope effect of Si NWs is shown in Fig. 1(f) together with the values of isotope effect of other bulk and low-dimensional materials, including 5% for GaAs [60], 31% for BP [10], 12% for BAs [20], 20% for Ge [61], 15% for GaN [62], 50% for diamond [63], 50% for monolayer MoS_2 [22], 50% for BN nanotube [19], and 108% for cubic BN [20]. The isotope enhancement of κ observed in ^{28}Si NWs is exceedingly high compared to all other materials reported.

It is known that thermal conductivity of NWs is very sensitive to not only the diameter, but also the surface roughness profile of the NWs [5,6]. The roughness of an NW is typically characterized by two parameters: the root-mean-square value of the NW's surface height fluctuation (Δ), and the correlation length (L) defined as the mean distance between roughness peaks, as illustrated in Fig. 2(a). According to the model by Martin *et al.* [6], which introduced roughness scattering rates derived from perturbation theory in Fermi's golden rule, a shorter correlation length drives the surface scattering of phonons toward a more diffusive process, leading to a suppression of κ below the so-called Casimir limit. The importance of correlation length in explaining thermal conductivity values below the Casimir limit in Si NWs was confirmed by

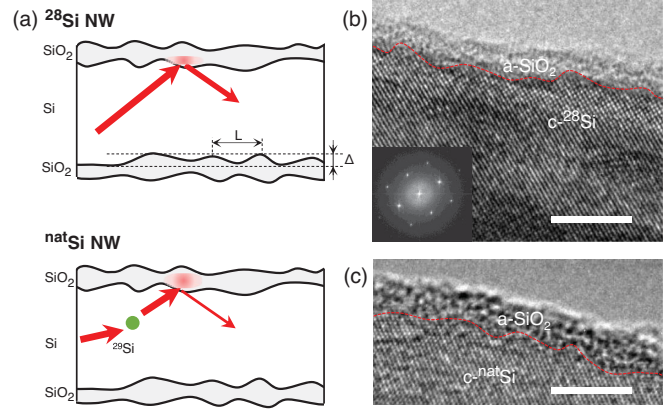


FIG. 2. Schematic of phonon scattering on the Si/SiO₂ interface and structural characterization of the Si NWs. (a) Schematic of phonon scattering on the *c*-Si core/*a*-SiO₂ shell interface of ^{28}Si and $^{\text{nat}}\text{Si}$ NWs, where Δ and L indicate the roughness amplitude and physical correlation length, respectively. Phonon scattering back to the Si core occurs dominantly on the interface in ^{28}Si NWs; in $^{\text{nat}}\text{Si}$ NWs, in contrast, a higher portion of phonon wave packets transmits into the *a*-SiO₂ shell, effectively shortening the correlation length and significantly reducing the thermal conductivity of the NW. (b) and (c) high-resolution TEM images and fast Fourier transform (FFT, inset) of a ^{28}Si NW and a $^{\text{nat}}\text{Si}$ NW. Surface roughness, highlighted by the red dashed line, is evident on the interface between the crystalline Si core (*c*-Si) and the native amorphous SiO₂ shell (*a*-SiO₂). Scale bar is 4 nm in both (b) and (c).

subsequent models based on nonequilibrium Green's functions [64], phonon Monte Carlo transport simulations [54], and experiments [7,65,66]. In our Letter, using high-resolution transmission electron microscopy (TEM), both $^{\text{nat}}\text{Si}$ and ^{28}Si NWs were determined to be single crystalline, as shown in Figs. 2(b) and 2(c). Indeed, unlike the smooth surface of Si NWs grown by the gold-catalyzed VPE method [25,26,67], these Si NWs have a rough surface with physical roughness on the order of several nanometers, surrounded by native, amorphous SiO₂ (*a*-SiO₂) with a thickness of $2 \sim 3$ nm. The rough morphology of these EE method synthesized Si NWs is consistent with what has been reported previously [5]. More importantly, the ^{28}Si and $^{\text{nat}}\text{Si}$ NWs do not have noticeable difference in the physical roughness and native SiO₂ thickness. This is not surprising because the ^{28}Si and $^{\text{nat}}\text{Si}$ NWs were both synthesized following the same EE recipe from two starting bulk materials that have the same doping type and nearly the same electrical conductivity. Their major difference, the different isotopic purities in the ^{28}Si and $^{\text{nat}}\text{Si}$ materials, is not expected to cause any difference in the EE process where the NWs and native SiO₂ form.

To elucidate the much stronger isotope effect than in the bulk, we employ a numerical model by solving the phonon Boltzmann transport equation with phonon dispersions determined from first principles. The total relaxation time

(τ_{tot}) is composed of that attributed to normal phonon-phonon (N), umklapp three-phonon (U), boundary (B), and isotope (iso) scatterings; that is, $\tau_{\text{tot}}^{-1} = \tau_N^{-1} + \tau_U^{-1} + \tau_B^{-1} + \tau_{\text{iso}}^{-1}$ [14,68]. In conventional “decoupled” models, we consider all these four scattering processes to be independent, hence simply add the bulk isotope scattering rates to the NW boundary scattering rate. This “decoupled” treatment results in virtually no discernible difference in κ between ^{28}Si and $^{\text{nat}}\text{Si}$ NWs in our calculation, and therefore is not able to explain the experimental results. This is because, unlike bulk Si where isotope scattering contributes about 10% to κ at room temperature, there is a more than tenfold increase in phonon scattering from boundaries in Si NWs, significantly dwarfing the contribution from isotope scattering. Therefore, a coupling between phonon-isotope scattering and phonon-boundary scattering has to be taken into account.

We propose a two-way interaction between the scattering by isotope mass disorder and that by boundary roughness disorder, termed as the “coupled” model in this Letter. First, the surface roughness combined with small diameters of the NWs results in strong boundary scattering, making the lifetime of phonons so short that we need to consider collisional broadening. Phonon lines are broadened according to the uncertainty principle. We capture this by replacing the energy-conserving δ function in the vibrational density of states (VDOS) by a homogeneously broadened Lorentzian distribution. The width of the distribution is related to the total scattering rate, $\gamma_b(\vec{q}) = \hbar/2\tau_{b,\text{tot}}(\vec{q})$ [69,70], to obtain the vibrational spectrum $D_b(\omega) = \int [d\vec{q}/(2\pi)^3] (1/\pi) \{ \gamma_b(\vec{q}) / [\omega - \omega_b(\vec{q}) + i\gamma_b(\vec{q})/2]^2 \}$. Using this broadened spectrum in place of the VDOS results in the NW isotope scattering rates shown by red dots in Fig. 3(a). This “coupled” isotope scattering rate is

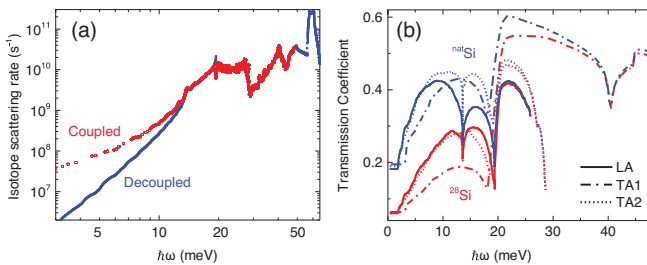


FIG. 3. Calculation of two-way coupled phonon dynamics involving surface roughness and isotope mass disorder in Si NWs. (a) Isotope scattering rates in a $^{\text{nat}}\text{Si}$ NW (90 nm diameter) by the “decoupled” model compared to the “coupled” model. In the energy range below 20 meV, the isotope scattering is remarkably enhanced by the presence of the surface SiO_2 . (b) Transmission coefficient spectrum of different phonon branches from c -Si to a - SiO_2 for ^{28}Si vs $^{\text{nat}}\text{Si}$. $^{\text{nat}}\text{Si}$ shows a higher transmission coefficient at low phonon energies, implying stronger roughness scattering at the Si/SiO_2 interface enhanced by isotopes.

significantly higher than the “decoupled” one at the same isotope composition, especially for phonon energies below ~ 15 meV. The coupling is also analogous to the drastic influence from vacancies on flexural phonons scattering in graphene [71]. However, even after this roughness-enhanced isotope scattering rate, it is still not sufficiently high to compete with the boundary scattering rate in NWs. Our calculations show that this “one-way coupling” between the two rates, where boundary roughness scattering enhances the isotope rate, in $^{\text{nat}}\text{Si}$ NWs only results in a 5% decrease in κ relative to ^{28}Si NWs with comparable diameter and roughness. Therefore, the opposite direction, the amplification of roughness scattering by the presence of isotopes, needs to be covered to constitute a “two-way coupled” model.

Indeed, it has been shown that across the SiC/GaN interface, interfacial phonon transfer is enhanced by the presence of 5% Ga isotopes, raising thermal boundary conductance by $\sim 20\%$ [72]. In our NWs, the SiO_2 shell is amorphous, where atoms completely lose long-range order and spatial correlation. Therefore, phonons transmitted into the a - SiO_2 shell encounter much stronger disorder scattering than if they are scattered back to the crystalline Si core at the Si/SiO_2 interface, as illustrated in Fig. 2(a). Physically, increasing the mass disorder with isotopes and the resultant stronger phonon scattering in the c -Si core leads to a better vibrational match with the a - SiO_2 shell, resulting in a higher transmission rate of phonon wave packets into the latter. As shown in Fig. 3(b), this is demonstrated by the higher phonon transmission coefficient across the $^{\text{nat}}\text{Si}/\text{SiO}_2$ interface than the $^{28}\text{Si}/\text{SiO}_2$ interface, as calculated by the full-band scattering-mediated diffuse mismatch model, obtained by combining the scattering-mediated acoustic mismatch model [31,43] with the full-band diffuse mismatch model (Supplemental Material, Note 2 [27]).

The higher phonon transmission coefficient in the $^{\text{nat}}\text{Si}$ NW to its SiO_2 shell gives rise to a shorter effective correlation length than in the ^{28}Si NW, despite that they have comparable roughness and hence similar physical correlation length along the Si/SiO_2 boundary. This feedback from the isotope scattering back to the boundary scattering is captured in our calculation by reducing the effective correlation length in the surface scattering rate from 6.5 ± 0.1 nm for the ^{28}Si NWs to 5.1 ± 0.1 nm for the $^{\text{nat}}\text{Si}$ NWs. Surface scattering is proportional to the roughness power spectrum [6] $S(k) = 2\pi\Delta^2L^2/(1 + L^2k^2)^{3/2}$, which quantitatively relates the scattering rate to the roughness Δ and the correlation length L [7], as described in Supplemental Material [27]. In addition, it constrains scattering to those in which the change in phonon wave vector, $k = |\vec{q} - \vec{q}'|$, is smaller than the inverse of the correlation length, as the power spectrum decays as $1/k^3$ when $kL \gg 1$ [45]. Consequently, roughness scattering is highly sensitive to the roughness power spectrum $S(k)$ [7],

which is characterized by a combination of Δ and L . A shorter L broadens the phase space for scattering [64], which increases the scattering rate and leads to lower thermal conductivity in ^{nat}Si NW. Using this shortened L , an $\sim 150\%$ isotope enhancement in κ was reproduced for ^{28}Si NWs of diameter of 74 nm, in agreement with the experimental results, as shown in Figs. 1(d) and 1(e).

The correlation length for phonon scattering is equal to the physical correlation length at the Si/SiO₂ interface only if all phonons are scattered back to the c -Si core without transmission into the a -SiO₂. In the other extreme, when phonons reaching the Si/SiO₂ interface all transmit into the a -SiO₂ shell, they would experience a total loss of long-range correlation. In between these two extrema, we loosely assume a linear interpolation and write the effective correlation length approximately as $L = L_{\text{physical}}(1 - t)$, where t represents the transmission coefficient of phonons at the Si/SiO₂ interface. Because the most significant portion of heat carriers are those phonons with energies below $k_B T$, we estimate from Fig. 3(b) the averaged transmission coefficient from ^{28}Si and ^{nat}Si to a -SiO₂ to be 0.2 and 0.4, respectively. This treatment leads to a ratio of L equal to approximately 1.3 between the cases of ^{28}Si and ^{nat}Si NWs, consistent with the values of $L = 6.5$ nm for ^{28}Si and 5.1 nm for ^{nat}Si that were used in the simulations to reach good agreement with the experimental data in Fig. 1(e). We note that a similar considerable effect of the presence of amorphous shell around ultrathin Si nanowires was found in nonequilibrium Greens' function [73] and molecular dynamics simulations [74].

In conclusion, we discovered that the thermal conductivity of isotopically enriched ^{28}Si NWs shows an unusual contrast, up to 2.5 times higher at room temperature, than that of ^{nat}Si NWs with similar diameters and surface morphology. This is in stark contrast to the behavior of bulk Si, where the isotopically enriched one is only 10% higher. Our Boltzmann transport model with first-principles phonon dispersion explains this giant isotope effect as a two-way coupling of boundary scattering and isotope scattering, correlated via transmission of phonons to the native amorphous SiO₂ shell in NWs. Our results reveal a mutual enhancement of two distinct scattering mechanisms and offer deep insights to heat transfer crossing or in presence of crystalline-amorphous interfaces. It also inspires potential applications of isotopically engineered semiconductors in the pursuit of efficient thermal management in Si-based modern microelectronics. From a broad perspective, ^{28}Si is appealing for high-fidelity quantum computation due to the absence of nuclear spin [75–77]. It is also important to show and understand the distinctly different phonon behavior in nanoscale ^{28}Si from the perspective of enhancing coherence in quantum systems.

This work was funded by the U.S. Department of Energy, Office of Science, Office of Basic Energy

Sciences, Materials Sciences and Engineering Division under Contract No. DE-AC02-05-CH11231 (EMAT program KC1201) (Materials processing, device fabrication, measurements, data analysis, and simulation). The thermal characterization of devices used facilities supported by U.S. NSF Grant No. ECCS-1953803. Z. A. acknowledges support from U.S. National Science Foundation (Grant No. 1902352). M. R. J. would like to acknowledge the David and Lucile Packard Foundation (Grant No. 2018-68049) for financial support. H. S. and B. S. acknowledge the support from NSFC No. 12004211 and Shenzhen Science and Technology Program No. RYX202007141-14643187. We thank Professor Eric Pop for helpful discussions.

J. W. and P. C. conceived the project. J. A. synthesized and characterized the bulk ^{28}Si crystals. P. C. produced the Si NWs from bulk Si crystals, fabricated the devices, and performed Raman and thermal measurement via suspended pads microdevices, with the help of L. J. M. S and M. R. J. contributed to TEM characterization. H. S. and B. S. measured the thermal conductivity of bulk Si by TDTR. Z. A. developed the numerical model and M. U. performed the calculations. All authors discussed and contributed to the preparation of the manuscript.

*To whom correspondence should be addressed.
zlatan.aksamija@utah.edu

Present address: Department of Materials Science and Engineering, University of Utah, Salt Lake City, Utah 84112, USA.

†To whom correspondence should be addressed.
wuj@berkeley.edu

- [1] L. Lindsay, D. A. Broido, and T. L. Reinecke, *Phys. Rev. Lett.* **111**, 025901 (2013).
- [2] S. Ghosh, I. Calizo, D. Teweldebrhan, E. P. Pokatilov, D. L. Nika, A. A. Balandin, W. Bao, F. Miao, and C. N. Lau, *Appl. Phys. Lett.* **92**, 151911 (2008).
- [3] R. Chen, A. I. Hochbaum, P. Murphy, J. Moore, P. D. Yang, and A. Majumdar, *Phys. Rev. Lett.* **101**, 105501 (2008).
- [4] D. Y. Li, Y. Y. Wu, P. Kim, L. Shi, P. D. Yang, and A. Majumdar, *Appl. Phys. Lett.* **83**, 2934 (2003).
- [5] A. I. Hochbaum, R. K. Chen, R. D. Delgado, W. J. Liang, E. C. Garnett, M. Najarian, A. Majumdar, and P. D. Yang, *Nature (London)* **451**, 163 (2008).
- [6] P. Martin, Z. Aksamija, E. Pop, and U. Ravaioli, *Phys. Rev. Lett.* **102**, 125503 (2009).
- [7] J. W. Lim, K. Hippalgaonkar, S. C. Andrews, A. Majumdar, and P. D. Yang, *Nano Lett.* **12**, 2475 (2012).
- [8] B. Yu *et al.*, in *International Electron Devices Meeting, San Francisco, Technical Digest* (IEEE, New York, 2002), pp. 251–254, [10.1109/IEDM.2002.1175825](https://doi.org/10.1109/IEDM.2002.1175825).
- [9] N. Singh, A. Agarwal, L. K. Bera, T. Y. Liow, R. Yang, S. C. Rustagi, C. H. Tung, R. Kumar, G. Q. Lo, N. Balasubramanian, and D.-L. Kwong, *IEEE Electron Device Lett.* **27**, 383 (2006).

- [10] Q. Y. Zheng, S. Li, C. H. Li, Y. C. Lv, X. Y. Liu, P. Y. Huang, D. A. Broido, B. Lv, and D. G. Cahill, *Adv. Funct. Mater.* **28**, 1805116 (2018).
- [11] F. Tian *et al.*, *Science* **361**, 582 (2018).
- [12] J. S. Kang, M. Li, H. A. Wu, H. Nguyen, and Y. J. Hu, *Science* **361**, 575 (2018).
- [13] S. Li, Q. Y. Zheng, Y. C. Lv, X. Y. Liu, X. Q. Wang, P. Huang, D. G. Cahill, and B. Lv, *Science* **361**, 579 (2018).
- [14] D. T. Morelli, J. P. Heremans, and G. A. Slack, *Phys. Rev. B* **66**, 195304 (2002).
- [15] L. Lindsay, D. A. Broido, and T. L. Reinecke, *Phys. Rev. B* **88**, 144306 (2013).
- [16] L. Lindsay, D. A. Broido, and T. L. Reinecke, *Phys. Rev. Lett.* **109**, 095901 (2012).
- [17] A. V. Inyushkin, A. N. Taldenkov, A. M. Gibin, A. V. Gusev, and H. J. Pohl, *Phys. Status Solidi C* **1**, 2995 (2004).
- [18] T. Ruf, R. W. Henn, M. Asen-Palmer, E. Gmelin, M. Cardona, H. J. Pohl, G. G. Devyatych, and P. G. Sennikov, *Solid State Commun.* **115**, 243 (2000).
- [19] C. W. Chang, A. M. Fennimore, A. Afanasiev, D. Okawa, T. Ikuno, H. Garcia, D. Y. Li, A. Majumdar, and A. Zettl, *Phys. Rev. Lett.* **97**, 085901 (2006).
- [20] K. Chen *et al.*, *Science* **367**, 555 (2020).
- [21] S. S. Chen, Q. Z. Wu, C. Mishra, J. Y. Kang, H. J. Zhang, K. J. Cho, W. W. Cai, A. A. Balandin, and R. S. Ruoff, *Nat. Mater.* **11**, 203 (2012).
- [22] X. F. Li *et al.*, *ACS Nano* **13**, 2481 (2019).
- [23] Q. R. Cai, D. Scullion, W. Gan, A. Falin, P. Cizek, S. Liu, J. H. Edgar, R. Liu, B. C. C. Cowie, E. J. G. Santos, and L. H. Li, *Phys. Rev. Lett.* **125**, 085902 (2020).
- [24] L. Lindsay and D. A. Broido, *Phys. Rev. B* **84**, 155421 (2011).
- [25] S. Mukherjee *et al.*, *Nano Lett.* **15**, 3885 (2015).
- [26] S. Mukherjee, U. Givan, S. Senz, M. de la Mata, J. Arbiol, and O. Moutanabbir, *Nano Lett.* **18**, 3066 (2018).
- [27] See Supplemental Material at <http://link.aps.org/supplemental/10.1103/PhysRevLett.128.085901> for experimental methods and theoretical calculations, which includes Refs. [28–54].
- [28] G. Gilat and L. J. Raubenheimer, *Phys. Rev.* **144**, 390 (1966).
- [29] P. Giannozzi *et al.*, *J. Phys. Condens. Matter* **29**, 465901 (2017).
- [30] Z. Aksamija and I. Knezevic, *Phys. Rev. B* **82**, 045319 (2010).
- [31] P. Reddy, K. Castelino, and A. Majumdar, *Appl. Phys. Lett.* **87**, 211908 (2005).
- [32] J. M. Ziman, *Electrons and Phonons* (Oxford University Press, London, 1960).
- [33] M. Upadhyaya, S. N. Khatami, and Z. Aksamija, *J. Mater. Res.* **30**, 2649 (2015).
- [34] K. Esfarjani, G. Chen, and H. T. Stokes, *Phys. Rev. B* **84**, 085204 (2011).
- [35] J. W. Ager, J. W. Beeman, W. L. Hansen, E. E. Haller, I. D. Sharp, C. Liao, A. Yang, M. L. W. Thewalt, and H. Riemann, *J. Electrochem. Soc.* **152**, G448 (2005).
- [36] P. B. Allen, *Phys. Rev. B* **88**, 144302 (2013).
- [37] A. Ward and D. A. Broido, *Phys. Rev. B* **81**, 085205 (2010).
- [38] J. A. Pascual-Gutierrez, J. Y. Murthy, and R. Viskanta, *J. Appl. Phys.* **102**, 034315 (2007).
- [39] D. G. Cahill, S. K. Watson, and R. O. Pohl, *Phys. Rev. B* **46**, 6131 (1992).
- [40] C. Wang, Y. Tamai, and N. Kuzuu, *J. Non-Cryst. Solids* **321**, 204 (2003).
- [41] M. Upadhyaya and Z. Aksamija, *Phys. Rev. B* **94**, 174303 (2016).
- [42] P. Giannozzi *et al.*, *J. Phys. Condens. Matter* **21**, 395502 (2009).
- [43] R. S. Prasher and P. E. Phelan, *J. Heat Transf. Trans. ASME* **123**, 1194 (2001).
- [44] G. S. Doerk, C. Carraro, and R. Maboudian, *ACS Nano* **4**, 4908 (2010).
- [45] D. Gelda, M. G. Ghossoub, K. Valavala, J. Ma, M. C. Rajagopal, and S. Sinha, *Phys. Rev. B* **97**, 045429 (2018).
- [46] S. B. Soffer, *J. Appl. Phys.* **38**, 1710 (1967).
- [47] K. F. Murphy, B. Piccione, M. B. Zanjani, J. R. Lukes, and D. S. Gianola, *Nano Lett.* **14**, 3785 (2014).
- [48] C. J. Foss and Z. Aksamija, *J. Appl. Phys.* **120**, 225104 (2016).
- [49] J. Carrete, L. J. Gallego, L. M. Varela, and N. Mingo, *Phys. Rev. B* **84**, 075403 (2011).
- [50] P. Carruthers, *Rev. Mod. Phys.* **33**, 92 (1961).
- [51] P. G. Klemens, *Solid State Phys.* **7**, 1 (1958).
- [52] G. A. Slack, *Solid State Phys.* **34**, 1 (1979).
- [53] Z. Aksamija and I. Knezevic, *Phys. Rev. B* **88**, 155318 (2013).
- [54] L. N. Maurer, Z. Aksamija, E. B. Ramayya, A. H. Davoody, and I. Knezevic, *Appl. Phys. Lett.* **106**, 133108 (2015).
- [55] S. Lee *et al.*, *Nat. Commun.* **6**, 8573 (2015).
- [56] P. Kim, L. Shi, A. Majumdar, and P. L. McEuen, *Phys. Rev. Lett.* **87**, 215502 (2001).
- [57] F. Widulle, T. Ruf, M. Konuma, I. Silier, M. Cardona, W. Kriegseis, and V. I. Ozhogin, *Solid State Commun.* **118**, 1 (2001).
- [58] P. V. Enkovich, V. V. Brazhkin, S. G. Lyapin, A. P. Novikov, A. V. Gusev, V. A. Gavva, M. F. Churbanov, and S. M. Stishov, *J. Phys. Commun.* **1**, 055005 (2017).
- [59] G. S. Doerk, C. Carraro, and R. Maboudian, *Phys. Rev. B* **80**, 073306 (2009).
- [60] V. Inyushkin, A. N. Taldenkov, A. Y. Yakubovskiy, A. V. Markov, L. Moreno-Garsia, and B. N. Sharonov, *Semicond. Sci. Technol.* **18**, 685 (2003).
- [61] M. AsenPalmer, K. Bartkowski, E. Gmelin, M. Cardona, A. P. Zhernov, A. V. Inyushkin, A. Taldenkov, V. I. Ozhogin, K. M. Itoh, and E. E. Haller, *Phys. Rev. B* **56**, 9431 (1997).
- [62] Q. Y. Zheng, C. H. Li, A. Rai, J. H. Leach, D. A. Broido, and D. G. Cahill, *Phys. Rev. Mater.* **3**, 014601 (2019).
- [63] T. R. Anthony, W. F. Banholzer, J. F. Fleischer, L. H. Wei, P. K. Kuo, R. L. Thomas, and R. W. Pryor, *Phys. Rev. B* **42**, 1104 (1990).
- [64] J. Sadhu and S. Sinha, *Phys. Rev. B* **84**, 115450 (2011).
- [65] K. Hippalgaonkar, B. Huang, R. Chen, K. Sawyer, P. Ercius, and A. Majumdar, *Nano Lett.* **10**, 4341 (2010).
- [66] M. G. Ghossoub, K. V. Valavala, M. Seong, B. Azeredo, K. Hsu, J. S. Sadhu, P. K. Singh, and S. Sinha, *Nano Lett.* **13**, 1564 (2013).
- [67] O. Moutanabbir, S. Senz, Z. Zhang, and U. Gosele, *Nano Today* **4**, 393 (2009).
- [68] J. Callaway, *Phys. Rev.* **113**, 1046 (1959).
- [69] S. I. Tamura, *Phys. Rev. B* **27**, 858 (1983).

- [70] J. Menendez and M. Cardona, *Phys. Rev. B* **29**, 2051 (1984).
- [71] G. Bouzerar, S. Thebaud, S. Pecorario, and C. Adessi, *J. Phys. Condens. Matter* **32**, 295702 (2020).
- [72] E. Lee and T.F. Luo, *Appl. Phys. Lett.* **112**, 011603 (2018).
- [73] N. Mingo and L. Yang, *Phys. Rev. B* **68**, 245406 (2003).
- [74] D. Donadio and G. Galli, *Phys. Rev. Lett.* **102**, 195901 (2009).
- [75] J. J. L. Morton, A. M. Tyryshkin, R. M. Brown, S. Shankar, B. W. Lovett, A. Ardavan, T. Schenkel, E. E. Haller, J. W. Ager, and S. A. Lyon, *Nature (London)* **455**, 1085 (2008).
- [76] S. Simmons, R. M. Brown, H. Riemann, N. V. Abrosimov, P. Becker, H. J. Pohl, M. L. W. Thewalt, K. M. Itoh, and J. J. L. Morton, *Nature (London)* **470**, 69 (2011).
- [77] A. M. Tyryshkin, S. Tojo, J. J. L. Morton, H. Riemann, N. V. Abrosimov, P. Becker, H.-J. Pohl, T. Schenkel, M. L. W. Thewalt, K. M. Itoh, and S. A. Lyon, *Nat. Mater.* **11**, 143 (2012).

Supplemental Material

Giant isotope effect of thermal conductivity in silicon nanowires

Penghong Ci^{1,2,3}, Muhua Sun⁴, Meenakshi Upadhyaya⁵, Houfu Song⁶, Lei Jin¹, Bo Sun^{6,7}, Matthew R. Jones⁴, Joel W. Ager^{1,2}, Zlatan Aksamija^{5,*,+}, Junqiao Wu^{1,2*}

¹ Department of Materials Science and Engineering, University of California, Berkeley, CA 94720, USA

² Materials Sciences Division, Lawrence Berkeley National Laboratory, Berkeley, CA 94720, USA

³ Institute for Advanced Study, Shenzhen University, Shenzhen 518060, China

⁴ Department of Chemistry, Rice University, Houston, TX 77005, USA

⁵ Department of Electrical and Computer Engineering, University of Massachusetts-Amherst, Amherst, MA 01003, USA

⁶ Tsinghua-Berkeley Shenzhen Institute (TBSI), Tsinghua University, Shenzhen 518055, China

⁷ Tsinghua Shenzhen International Graduate School and Guangdong Provincial Key Laboratory of Thermal Management Engineering and Materials, Shenzhen 518055, China

⁺ Current address: Department of Materials Science and Engineering, University of Utah, Salt Lake City, UT 84112, USA

* To whom correspondence should be addressed: wuj@berkeley.edu, zlatan.aksamija@utah.edu

List of contents:

Methods.

Supplemental Figure S1. Characterization of bulk ²⁸Si crystal.

Supplemental Figure S2. Interfacial thermal conductance characterization.

Supplemental Figure S3. Raman thermography method applied to suspended Si NWs to estimate the thermal resistance of the system.

Supplemental Figure S4. Heat transport measurement of bulk ²⁸Si and ^{nat}Si crystals with TDTR at room temperature.

Supplemental Figure S5. Relative contribution to total κ in ²⁸Si NWs and ^{nat}Si NWs (both have 90 nm diameter) calculated by the ‘one-way coupling’ model.

Note1. Additional details of scattering rates and numerical calculations.

Note 2. Scattering-mediated diffuse mismatch model.

Methods

Materials preparation.

Dislocation-free, isotopically enriched ^{28}Si (99.92%) single crystals were produced from polycrystalline Si by the float-zone technique [1]. Afterwards, using an electroless etching (EE) method, both the ^{28}Si crystals and commercial $^{\text{nat}}\text{Si}$ (MTI Corp.) crystals with similar n-type conductivity ($\sim 10 \Omega\cdot\text{cm}$) were etched into NWs in an aqueous solution of 0.02M AgNO_3 and 5M HF acid for one hour [2]. Due to the galvanic displacement during reduction of Ag^+ , the bulk silicon surface is oxidized and subsequently etched by HF; in the meantime, the formed Ag nanoparticles on the surface delimits the spatial extent of the oxidation and become the active cathode by electron transfer from the underlying wafer. After the reaction, the Ag dendrites were finally washed off by nitric acid for at least one hour to yield clean Si NWs.

Si NW characterization.

TEM characterization for the natural and isotope Si nanowires was conducted with a field-emission transmission electron microscope (JEOL, model JEM-2100F) at an acceleration voltage of 200kV. HRTEM images were acquired at a dose rate of $\sim 1000 \text{ e}/\text{\AA}^2\cdot\text{s}$ with an exposure time of 1 sec per image. Raman spectra were measured by a Raman spectrometer (Renishaw Inc.) with a 488 nm laser as the excitation source, and the laser power was determined by a laser power meter (FieldMate, Coherent Inc.)

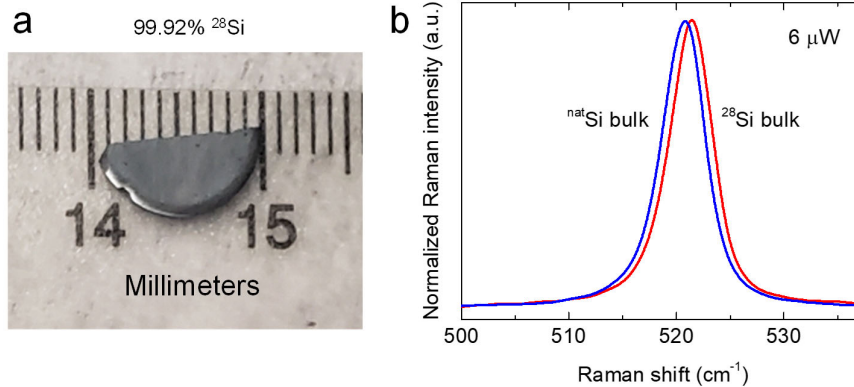
Thermal conductivity measurements.

Thermal conductivity of the Si NWs was measured by suspended pad microdevices in a vacuum chamber ($< 10^6$ torr). The two SiN_x pads were patterned with Pt lines on top and suspended with flexible arms away from a Si substrate, as shown in the optical image in Fig. 1a. After transferring an individual NW to bridge the two suspended pads with a sharp probe tip, Pt was deposited by FIB (FEI Company) to bond the Si NW onto the underlying Pt electrodes to maximally eliminate contact thermal resistance. Electrical current was sent to the Pt micro-heater to heat the hot pad, and the electric resistance of the thermometers on both pads as measured via the four-probe method. By doing so, the Joule heating power (Q) in the micro-heater and temperature rise of the hot (ΔT_h) and cool pad (ΔT_c) were obtained, yielding the thermal conductance, $G = (Q \times \Delta T_c) / (\Delta T_h^2 - \Delta T_c^2)$. The length and diameter of the NWs in this study were measured by scanning electron microscopy to ultimately allow determination of the thermal conductivity.

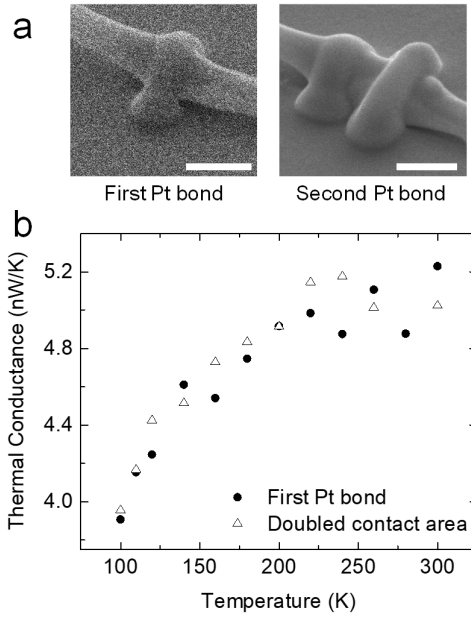
Calculations.

We simulate phonon transport in Si nanowires and obtain the dependence of thermal conductivity on temperature, isotope scattering, and boundary roughness scattering employing the phonon Boltzmann transport equation (pBTE) approach. We solve the time-independent pBTE in the relaxation time approximation (RTA) to obtain the steady-state distribution function, which is used to determine the lattice thermal conductivity as [3] $\kappa(T) = \vec{Q} / \nabla T = \sum_b \sum_{\vec{q}} \hbar \omega_b(\vec{q}) \tau_b(\vec{q}) (\vec{v}_b(\vec{q}) \cdot \hat{t})^2 \frac{\partial N^0}{\partial T}$, where \hat{t} is a unit vector in the direction of the temperature gradient and $\tau_b(\vec{q})$ is the total relaxation time. The phonon energy $\hbar \omega_b(\vec{q})$ is obtained from first principles using density functional perturbation theory as implemented in the code Quantum ESPRESSO [4,5], using parameters described in our earlier work [6].

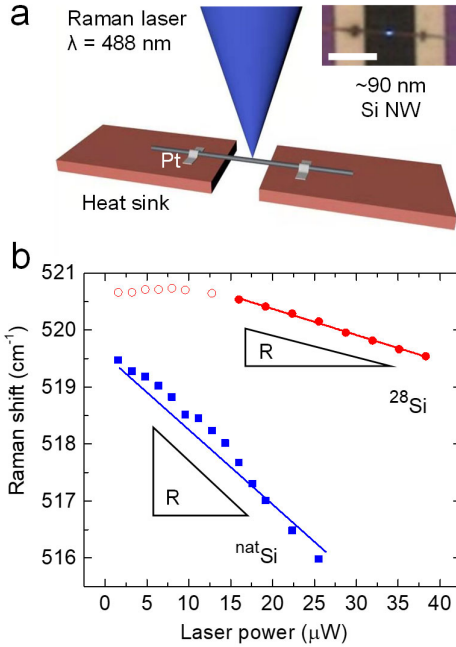
In our solution to the pBTE, we include a boundary roughness scattering (B) relaxation rate $\tau_{b,B}^{-1}$ obtained from perturbation theory derived in our previous work [7]. This momentum-dependent rate depends on the change in the phonon wavevector $k = |\vec{q} - \vec{q}'|$ between the initial state \vec{q} before and the final state \vec{q}' after scattering, boundary correlation length L , and surface rms roughness Δ through the roughness power spectrum [8] as described below in the Supplemental Information Note 1. Since our perturbation-theory approach starts from a bulk phonon dispersion, discretized for numerical calculations into a $40 \times 40 \times 40$ mesh, it is accurate for nanowires with diameters larger than about 40 unit cells across, corresponding to an equivalent diameter of roughly 20 nm (Si lattice spacing is 0.543 nm). Below this limit, phonon modes may experience confinement [9], which affects phonon velocities, vDOS, heat capacity, and scattering rates. The perturbation-theory approach can over-predict boundary scattering rates when diameter is small and roughness is very large [10], resulting in a large roughness/diameter ratio Δ/D . In this work, all the nanowires have diameters exceeding 50 nm, well above the limit where confinement effects emerge, and a roughness below 5 nm, so that the ratio $\Delta/D < 0.1$ remains small, and perturbation theory applies.



Supplemental Figure S1. Characterization of bulk ^{28}Si crystal. **a**, Optical image of isotopically enriched ^{28}Si (99.92%) crystal for electroless etching to produce NWs. **b**, Raman spectra as signatures of silicon isotope purities in bulk crystals at room temperature. The Raman spectrum of $^{\text{nat}}\text{Si}$ bulk shows a redshift with respect to that of ^{28}Si bulk, consistent with the Raman results in NWs.

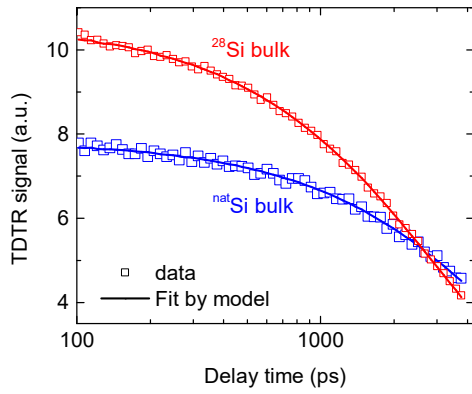


Supplemental Figure S2. Interfacial thermal conductance characterization. a, SEM images of the first and second Pt bonding by FIB. **b**, Thermal conductance of a Si NW before and after doubling the bonding area with the suspended pads, showing differences within the error bar, and implying a negligible interfacial thermal resistance. Scale bars are 400 nm.

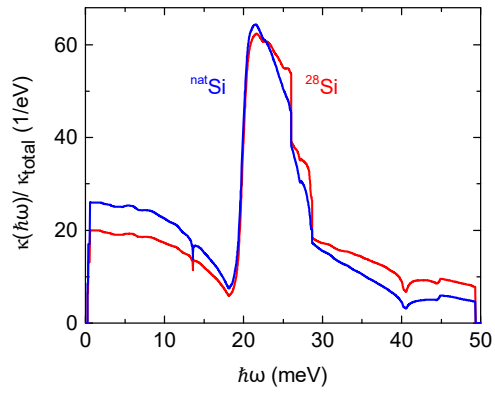


Supplemental Figure S3. Raman thermography method applied to suspended Si NWs to estimate the thermal resistance of the system. **a**, Schematic and optical image (inset) of the experimental setup. The laser beam position is illustrated by the blue spot in the inset. Scale bar: 5 μm . **b**, Raman shift as a function of Raman laser power, where the thermal resistance (R) of the system can be extracted from the slope of the data.

The total thermal resistance (R) of the system can be written in terms of Raman shift (ω) vs. laser power (P) as $R = \partial T / \partial P = 1 / \chi_T \cdot \frac{\partial \omega}{\partial P}$, where χ_T is the gradient of first-order Raman shift vs. temperature, a constant of -0.022cm^{-1} for Si [11,12]. Thus, considering the negligible air convection and contact thermal resistance between Si NWs and Pt metal (see Supplemental Fig. S2), the thermal conductance ratio ($G_{28\text{Si}} / G_{\text{natSi}}$) can be estimated from the inverse ratio of slope in the Raman shift vs. laser power curve ($\left| \frac{\partial \omega}{\partial P} \right|_{\text{natSi}} / \left| \frac{\partial \omega}{\partial P} \right|_{28\text{Si}}$), as shown in Fig. S3b. Combined with the dimensions of NWs obtained via SEM, we extracted the isotope effect of κ in NWs with the diameter of $\sim 90 \text{nm}$ to be $\sim 180\%$, consistent with the isotope enhancement ($\sim 130\%$) by suspended pad micro-devices. Note that the deviation may arise from large errors of the Raman thermometry measurements.



Supplemental Figure S4. Thermal conductivity measurements of bulk ^{28}Si and $^{\text{nat}}\text{Si}$ crystals using TDTR method at room temperature. κ of bulk ^{28}Si and $^{\text{nat}}\text{Si}$ crystals were determined to be 157 and 144 W/m·K, respectively, leading to a small isotope effect of $\sim 10\%$, consistent with reports in literature [13,14].



Supplemental Figure S5. Relative contribution to total κ in ^{28}Si NWs and ^{nat}Si NWs (both are 90 nm diameter) calculated by the “one-way coupling” model. The largest difference occurs in the sub-20 meV energy range where isotope scattering is enhanced by the interaction with roughness, consistent with the calculated isotope scattering rates in Fig. 3a.

Note 1. Additional details of scattering rates and numerical calculations

We simulate phonon transport in Si nanowires and obtain the dependence of thermal conductivity on temperature, isotope scattering, and boundary roughness scattering employing the phonon Boltzmann transport equation (pBTE) approach. We solve the time-independent pBTE in the relaxation time approximation (RTA) to obtain the steady-state distribution function, which is used to determine the lattice heat conductivity. In the steady state, the time-independent pBTE is given in the RTA as [15]

$$\vec{v}_b(\vec{q}) \cdot \nabla_{\vec{r}} N_{b,\vec{q}}(\vec{r}) = -\frac{N_{b,\vec{q}}(\vec{r}) - N_{b,\vec{q}}^0(T)}{\tau_{b,tot}(\vec{q})} \quad (S1)$$

where, $\vec{v}_{b,\vec{q}}$ is the phonon velocity vector and $N_{b,\vec{q}}^0(T)$ is the equilibrium Bose-Einstein phonon distribution, which is a function of the phonon branch b and wave vector \vec{q} via its energy dependence, and position in 3D space through its dependence on temperature. For small perturbations near equilibrium, we expand the steady-state distribution function $N_{b,\vec{q}}(\vec{r}) = N_{b,\vec{q}}^0(T) + n_{b,\vec{q}}(\vec{r})$ and obtain the spatial gradient as $\nabla_{\vec{r}} \vec{N}_{b,\vec{q}}(\vec{r}) \approx \nabla_{\vec{r}} T(\vec{r}) \partial N^0 / \partial T$. This allows us to solve the pBTE in the RTA for the non-equilibrium component of the distribution as $n_{b,\vec{q}}(\vec{r}) = \tau_{b,tot}(\vec{q}) \vec{v}_b(\vec{q}) \cdot \nabla_{\vec{r}} T(\vec{r}) \partial N^0 / \partial T$. The thermal conductivity is then calculated as [3]

$$\kappa_{RTA}(T) = \frac{\bar{Q}}{\nabla T} = \sum_b \sum_{\vec{q}} \hbar \omega_b(\vec{q}) \tau_{b,tot}(\vec{q}) [\vec{v}_b(\vec{q}) \cdot \hat{t}]^2 \frac{\partial N^0}{\partial T}, \quad (S2)$$

where \hat{t} is a unit vector in the direction of the temperature gradient and $\tau_{b,tot}(\vec{q})$ is the total relaxation time. The phonon energy $\hbar \omega_b(\vec{q})$ is obtained from first principles using density functional perturbation as described in Methods.

We calculate the total relaxation time $\tau_{b,tot}(\vec{q})$ for a phonon in mode b and with wave vector \vec{q} , by considering all the intrinsic scattering mechanisms occurring in the interior of the material, including both non-resistive normal anharmonic phonon–phonon (N), resistive Umklapp (U) three-phonon and isotope (Iso) scattering, in addition to branch- and momentum-dependent boundary scattering time such that

$$\frac{1}{\tau_{b,tot}(\vec{q})} = \frac{1}{\tau_{b,B}(\vec{q})} + \frac{1}{\tau_{b,N}(\vec{q})} + \frac{1}{\tau_{b,U}(\vec{q})} + \frac{1}{\tau_{Iso}(\omega)}. \quad (S3)$$

The contribution due to isotopic variation is temperature independent and the energy dependence is given as [16]

$$\tau_{iso}^{-1}(\omega) = \frac{\pi V_0}{6} X_{Si} \omega^2 D(\omega), \quad (S4)$$

where V_0 is the volume per atom and the scattering parameter due to mass-fluctuation $X_{Si} = \sum_i f_i (1 - m_i / \bar{m})^2$ with $\bar{m} = \sum_i f_i m_i$, m_i is the atomic mass and f_i is the fractional atomic natural abundance of the i th isotope. $D(\omega)$ is the total vibrational density of states (vDOS) of Si, obtained by summing the contributions from all the branches $D(\omega) = \sum_b \int \frac{d\vec{q}}{(2\pi)^3} \delta[\omega - \omega_b(\vec{q})]$. In bulk Si, the volume integral of the energy-conserving δ function over the whole first Brillouin zone is calculated from the full phonon dispersion using the method of Gilat and Raubenheimer [17], where the closed constant-energy surface traced out by the δ function is discretized into a cubic mesh. Then the area of the intersection between the constant-energy contour and each cube is computed based on the angle of the surface normal, given by the gradient of the dispersion $\vec{v}_b(\vec{q}) = \nabla_{\vec{q}} \omega_b(\vec{q})$, obtained from the dispersion by finite differences. In the NWs, we use the approach detailed in the main paper to introduce collisional broadening by replacing the energy-conserving delta function with a Lorentzian peak.

The resistive anharmonic phonon–phonon scattering rate is calculated in the standard approximation for dielectric crystals [18,19]

$$\tau_{b,U}^{-1}(\vec{q}) = \frac{\hbar\gamma_b^2}{\bar{M}\Theta_b\bar{v}_b^2}\omega_b^2(\vec{q})Te^{-\Theta_b/3T} \quad (\text{S5})$$

where the speed of sound \bar{v}_b of each branch b is determined from the average slope of its dispersion curve near the Γ point, and \bar{M} is the average atomic mass. The Grüneissen parameter γ_b was obtained for each branch from the phonon dispersion and has the value of 1.1 for the longitudinal acoustic branch and 0.6 for the two transverse acoustic branches. The exponential term $e^{-\Theta_b/3T}$ in the temperature dependence controls the onset of resistive Umklapp scattering for each phonon branch through the branch-specific Debye temperature $\Theta_b^2 = \frac{5\hbar^2 \int \omega^2 D_b(\omega) d\omega}{3k_B^2 \int D_b(\omega) d\omega}$ where $D_b(\omega)$ is the vDOS calculated for each phonon branch b from the full dispersion [20]. This way, the temperature dependence of the contribution from each phonon branch to the total thermal conductivity is correctly represented.

The normal scattering rate is given by the general expression

$$\tau_{b,N}^{-1}(\vec{q}) = B_N \omega_b^{a_N}(\vec{q}) T^{b_N}, \quad (\text{S6})$$

where the prefactor gathers all the constants into $B_N = \hbar\gamma_b^2 \left(\frac{k_B}{\hbar}\right)^{b_N} \frac{V^{(a_N+b_N-2)/3}}{\bar{M}\bar{v}_b^{(a_N+b_N)}}$ and the integer

frequency and temperature exponents a_N and b_N are taken to obey $a_N + b_N = 5$ in 3D materials [19]. First-principles calculations of anharmonic scattering rates have suggested a value of $a_N = 2$ [21,22]. Since normal scattering conserves phonon momentum, thermal conductivity computed by Eq. S2 in the presence of both normal and umklapp scattering needs to be corrected to account for the hydrodynamic contribution; we accomplish this using P. B. Allen's "Improved Callaway Model" (ACM) [23]. In the ACM, an additional contribution is added to $\kappa_{RTA}(T)$ from Eq. S2, so that the total thermal conductivity is given by $\kappa(T) = \kappa_{RTA}(T) + \lambda_1(T)\lambda_2(T)/\lambda_3(T)$. The correction terms in this equation are

$$\begin{aligned} \lambda_1(T) &= \sum_b \sum_{\vec{q}} \tau_{b,tot}(\vec{q}) [\vec{v}_b(\vec{q}) \cdot \hat{t}] (\vec{q} \cdot \hat{t}) \frac{\partial N^0}{\partial T}, \\ \lambda_2(T) &= \sum_b \sum_{\vec{q}} [\tau_{b,tot}(\vec{q})/\tau_{b,N}(\vec{q})] [\vec{v}_b(\vec{q}) \cdot \hat{t}] (\vec{q} \cdot \hat{t}) \frac{\partial N^0}{\partial T} \text{ and} \\ \lambda_3(T) &= \sum_b \sum_{\vec{q}} q^2 / [\hbar\omega_b(\vec{q})] [1 - \tau_{b,tot}(\vec{q})/\tau_{b,N}(\vec{q})] \frac{\partial N^0}{\partial T}. \end{aligned}$$

However, we find that the presence of strong boundary roughness scattering, which is momentum-randomizing and therefore resistive like Umklapp scattering, severely reduces the additional correction $\lambda_1(T)\lambda_2(T)/\lambda_3(T)$. Unlike in bulk Si, this contribution was found to be negligible in all of our calculations.

Previous works on phonon transport in nanowires relied on variations of the Fuchs-Sondheimer (FS) approach, which utilizes a specularity parameter to capture the fraction of phonons (or electrons) that undergo mirror-like reflection at the boundary. The rest are typically taken to be diffusely scattered in the FS model, although Soffer [24] and Ziman [25] extended the model to include the dependence of specularity on phonon momentum, rms roughness amplitude, and even the effects of correlation along the surface, albeit only qualitatively at the time. While the original FS model relied on a linear isotropic dispersion to perform angular averaging, the FS model has been extended to include the full phonon dispersion and momentum-dependent specularity. The resulting full-dispersion (FD) FS model has been employed to understand phonon transport in Si thin films [16], Si/Ge superlattices [26], and SiGe alloy NWs [27] where the surfaces/boundaries/interfaces could be described as locally flat planes with small atomic-scale perturbations due to roughness.

However, for objects with large roughness exceeding 1 nm, such as intentionally roughened or etched NWs, the specularity parameter becomes zero for nearly all phonons and the effect of roughness on reducing thermal conductivity saturates, resulting in values of thermal conductivity far

exceeding those observed in our work and in several previous measurements [2,28]. This saturation is sometimes called the Casimir limit [29], in which phonons essentially travel nearly ballistically from boundary to boundary and scatter diffusely at each boundary, resulting in a phonon mean free path (mfp) approximately equal to the smallest dimension; in NWs, the smallest dimension is the diameter. Then, comparing the NW diameter, here 70-90 nm, to the phonon mfp in bulk Si, around 300 nm, the Casimir limit leads to a thermal conductivity around 3-4 times smaller than bulk Si—a reduction from ~ 150 W/m-K to 40-50 W/m-K whereas our measurements are below 10, consistent with the literature values on rough Si NWs [2,28].

In order to go beyond the Casimir limit and capture the role of large boundary roughness exceeding 1 nm, while also including the crucial role of correlation length, we turn to the boundary roughness scattering rate derived in Ref. [7]. In our solution to the pBTE we include a boundary roughness scattering (B) relaxation rate $\tau_{b,B}^{-1}$ obtained from perturbation theory using Fermi's "golden rule"

$$\tau_{b,B}^{-1}(\vec{q}) = \frac{2\pi}{\hbar} \sum_{b'} \int \frac{d\vec{q}'}{(2\pi)^3} |\langle \vec{q} | H' | \vec{q}' \rangle|^2 \delta[\omega_b(\vec{q}) - \omega_{b'}(\vec{q}')]. \quad (S7)$$

The perturbation Hamiltonian H' was derived in our previous work [7] where we related it to the power spectrum of the roughness $S(\vec{q} - \vec{q}')$, which is the two-dimensional Fourier transform of the surface height autocorrelation function $C(\vec{r}) = \langle h(\vec{r}')h(\vec{r}' + \vec{r}) \rangle$. Here $h(\vec{r}')$ is the height function representing the deviation of the boundary from a perfectly flat surface. A self-affine surface is typically described by an exponential autocorrelation, resulting in a power spectrum $S(k) = 2\pi\Delta^2 L^2 / (1 + L^2 k^2)^{3/2}$ where $k = |\vec{q} - \vec{q}'|$ is the change in the phonon wavevector between the initial state \vec{q} before and the final state \vec{q}' after scattering. Numerical evaluation of the integral in Eq. (S6) above proceeds in the same way as described for the vDOS but multiplied by the transition matrix element $|\langle \vec{q} | H' | \vec{q}' \rangle|^2$.

The current model is very much in line with our work in [7]: both use the same boundary roughness scattering model, very similar roughness and correlation length values for naturally occurring Si, and the thermal conductivity measured herein is comparable with the experimental data that calculations in earlier work [7] were compared to, apart from some slight differences in NW diameter. However, earlier work did not consider any isotope effect; the diameter and correlation length were chosen empirically based on agreement with experimental data. Therefore, our current model, incorporating the impact of isotope scattering and phonon transmission into amorphous shell, is an extended version of our previous model in [7] and in good agreement with our experimental results on ^{28}Si NWs and $^{\text{nat}}\text{Si}$ NWs.

Note 2. Scattering-mediated diffuse mismatch model

To capture the impact of scattering near the interface on the interfacial transmission coefficient, we start from the scattering mediated acoustic mismatch model (SM-AMM) derived by Prasher and Phelan [30]. Since the interface between the Si NW and the SiO₂ layer is very rough, momentum is not conserved in the transmission. Since the conservation of lateral momentum is a central feature of the AMM model, we create a novel scattering-mediated diffuse mismatch model (SM-DMM) by combining the SM-AMM of the full-dispersion diffuse mismatch model (DMM), first described by Reddy et al. [31]. In the SM-AMM, scattering in the vicinity of the interface is incorporated through the complex-valued phonon wave-vector, where the imaginary component represents damping of the phonon wave by scattering events in the material in the vicinity of the interface. They arrive at the complex speed of motion of phonon waves

$$\tilde{v}_b(\vec{q}) = \vec{v}_b(\vec{q})/(a + ib), \quad (\text{S8})$$

where the coefficients in Si are $a_{Si} = \sqrt{1 + \left(\frac{1}{2\tau_{b,tot}(\vec{q})\omega_b(\vec{q})}\right)^2}$ and $b_{Si} = \frac{1}{2\tau_{b,tot}(\vec{q})\omega_b(\vec{q})}$, while the relaxation time $\tau_{b,tot}(\vec{q})$ was given in Eq. S3 and the angular phonon frequency $\omega_b(\vec{q})$ was obtained from first principles as described in Methods. On the other hand, for the amorphous SiO₂ we use the relaxation time from the Cahill-Pohl (CP) minimal thermal conductivity model [32]. In the CP model, the relaxation time of vibrational modes in the amorphous material is set equal to the smallest possible value, which is one half of their vibrational period $\tau = 1/(2\omega)$, resulting in coefficients $a_{SiO_2} = \sqrt{2}$ and $b_{SiO_2} = 1$. The speed of sound in SiO₂ is taken to be isotropic and have a value of $v_{SiO_2} = 5800$ m/s.

In our SM-DMM model, we take the complex-valued phonon velocity from the SM-AMM, previously derived by Prasher and repeated here in Eq. S8, to capture the impact of scattering in the Si near the interface. Once the complex phonon velocity is computed for each phonon mode from its relaxation time according to Eq. S8, then we compute the transmission coefficient according to standard full-dispersion DMM expression

$$\alpha_{Si \rightarrow SiO_2}(\omega) = \left| \frac{\tilde{v}_{SiO_2} D_{SiO_2}(\omega)}{\Omega_{Si} \sum_b \int d\vec{q} \tilde{v}_b(\vec{q}) \cdot \hat{n} \delta[\omega - \omega_b(\vec{q})] + \tilde{v}_{SiO_2} D_{SiO_2}(\omega)} \right|. \quad (\text{S9})$$

In Eq. S9, \hat{n} is the unit vector normal to the surface and perpendicular to the transport direction \hat{t} along the wire and Ω_{Si} is the volume of the Brillouin zone of Si. This expression can be readily derived from the principle of detailed balance combined with the assumption that a phonon striking the interface is scattered diffusely, so that the total number of phonons of angular frequency ω arriving from Si that are transmitted through the interface equals the number of phonons arriving from SiO₂ that are reflected back

$$\{\Omega_{Si} \sum_b \int d\vec{q} \tilde{v}_b(\vec{q}) \cdot \hat{n} \delta[\omega - \omega_b(\vec{q})]\} |\alpha_{Si \rightarrow SiO_2}(\omega)| = \tilde{v}_{SiO_2} D_{SiO_2}(\omega) |1 - \alpha_{Si \rightarrow SiO_2}(\omega)| \quad (\text{S10})$$

The transmission of phonons from SiO₂ back to Si is equally important and can be derived by swapping the two materials in the derivation. Analogously, it is given by

$$\alpha_{SiO_2 \rightarrow Si}(\omega) = \left| \frac{\Omega_{Si} \sum_b \int d\vec{q} \tilde{v}_b(\vec{q}) \cdot \hat{n} \delta[\omega - \omega_b(\vec{q})]}{\Omega_{Si} \sum_b \int d\vec{q} \tilde{v}_b(\vec{q}) \cdot \hat{n} \delta[\omega - \omega_b(\vec{q})] + \tilde{v}_{SiO_2} D_{SiO_2}(\omega)} \right|. \quad (\text{S11})$$

Ultimately, the symmetry condition on the two transmission coefficients

$$\alpha_{Si \rightarrow SiO_2}(\omega) \{\Omega_{Si} \sum_b \int d\vec{q} \tilde{v}_b(\vec{q}) \cdot \hat{n} \delta[\omega - \omega_b(\vec{q})]\} = \tilde{v}_{SiO_2} D_{SiO_2}(\omega) \alpha_{SiO_2 \rightarrow Si}(\omega) \quad (\text{S12})$$

is obeyed, where the quantity $\tilde{M}_{Si}(\omega) = \Omega_{Si} \sum_b \int d\vec{q} \tilde{v}_b(\vec{q}) \cdot \hat{n} \delta[\omega - \omega_b(\vec{q})]$ is sometimes referred to as the ‘‘channel number.’’ Using it, the transmission coefficients can be more compactly written as $\alpha_{1 \rightarrow 2}(\omega) = |\tilde{M}_2(\omega)/[\tilde{M}_1(\omega) + \tilde{M}_2(\omega)]|$ with the numbers in the subscript representing either Si or SiO₂, depending on the direction.

The integrals over the Brillouin zone are computed using the same numerical approach as described for our vDOS (Eq. S4) and scattering rates, but instead weighted by the normal component of the complex velocity $\tilde{v}_b(\vec{q}) \cdot \hat{n}$. The vibrational density of states of amorphous SiO₂ was obtained from molecular dynamics calculations given in Ref. [33] and normalized to obtain 3 states, representing

the 3 degrees of freedom, per atom. To obtain the transmission coefficients from ^{28}Si and $^{\text{nat}}\text{Si}$, we use their respective scattering rates in computing the complex phonon velocity.

- [1] J. W. Ager, J. W. Beeman, W. L. Hansen, E. E. Haller, I. D. Sharp, C. Liao, A. Yang, M. L. W. Thewalt, and H. Riemann, *J. Electrochem. Soc.* **152**, G448 (2005).
- [2] A. I. Hochbaum, R. K. Chen, R. D. Delgado, W. J. Liang, E. C. Garnett, M. Najarian, A. Majumdar, and P. D. Yang, *Nature* **451**, 163 (2008).
- [3] P. G. Klemens, *Solid State Physics* **7**, 1 (1958).
- [4] P. Giannozzi *et al.*, *Journal of Physics-Condensed Matter* **21**, 395502 (2009).
- [5] P. Giannozzi *et al.*, *Journal of Physics-Condensed Matter* **29**, 465901 (2017).
- [6] C. J. Foss and Z. Aksamija, *J. Appl. Phys.* **120**, 225104 (2016).
- [7] P. Martin, Z. Aksamija, E. Pop, and U. Ravaioli, *Phys. Rev. Lett.* **102**, 125503 (2009).
- [8] D. Gelda, M. G. Ghossoub, K. Valavala, J. Ma, M. C. Rajagopal, and S. Sinha, *Physical Review B* **97**, 045429 (2018).
- [9] J. A. Pascual-Gutierrez, J. Y. Murthy, and R. Viskanta, *J. Appl. Phys.* **102**, 034315 (2007).
- [10] J. Carrete, L. J. Gallego, L. M. Varela, and N. Mingo, *Physical Review B* **84**, 075403 (2011).
- [11] K. F. Murphy, B. Piccione, M. B. Zanjani, J. R. Lukes, and D. S. Gianola, *Nano Lett.* **14**, 3785 (2014).
- [12] G. S. Doerk, C. Carraro, and R. Maboudian, *Acs Nano* **4**, 4908 (2010).
- [13] A. V. Inyushkin, A. N. Taldenkov, A. M. Gibin, A. V. Gusev, and H. J. Pohl, *Physica Status Solidi C* **1**, 2995 (2004).
- [14] T. Ruf, R. W. Henn, M. Asen-Palmer, E. Gmelin, M. Cardona, H. J. Pohl, G. G. Devyatych, and P. G. Sennikov, *Solid State Commun.* **115**, 243 (2000).
- [15] P. Carruthers, *Reviews of Modern Physics* **33**, 92 (1961).
- [16] Z. Aksamija and I. Knezevic, *Physical Review B* **82**, 045319 (2010).
- [17] G. Gilat and L. J. Raubenheimer, *Physical Review* **144**, 390 (1966).
- [18] M. Upadhyaya, S. N. Khatami, and Z. Aksamija, *J. Mater. Res.* **30**, 2649 (2015).
- [19] D. T. Morelli, J. P. Heremans, and G. A. Slack, *Physical Review B* **66**, 195304 (2002).
- [20] G. A. Slack, *Solid state physics* **34**, 1 (1979).
- [21] A. Ward and D. A. Broido, *Physical Review B* **81**, 085205 (2010).
- [22] K. Esfarjani, G. Chen, and H. T. Stokes, *Physical Review B* **84**, 085204 (2011).
- [23] P. B. Allen, *Physical Review B* **88**, 144302 (2013).
- [24] S. B. Soffer, *J. Appl. Phys.* **38**, 1710 (1967).
- [25] J. M. Ziman, *Electrons and phonons* (Oxford University Press, London, 1960).
- [26] Z. Aksamija and I. Knezevic, *Physical Review B* **88**, 155318 (2013).
- [27] M. Upadhyaya and Z. Aksamija, *Physical Review B* **94**, 174303 (2016).
- [28] J. W. Lim, K. Hippalgaonkar, S. C. Andrews, A. Majumdar, and P. D. Yang, *Nano Lett.* **12**, 2475 (2012).
- [29] L. N. Maurer, Z. Aksamija, E. B. Ramayya, A. H. Davoody, and I. Knezevic, *Appl. Phys. Lett.* **106**, 133108 (2015).
- [30] R. S. Prasher and P. E. Phelan, *Journal of Heat Transfer-Transactions of the Asme* **123**, 105 (2001).
- [31] P. Reddy, K. Castelino, and A. Majumdar, *Appl. Phys. Lett.* **87**, 211908 (2005).
- [32] D. G. Cahill, S. K. Watson, and R. O. Pohl, *Physical Review B* **46**, 6131 (1992).
- [33] C. Wang, Y. Tamai, and N. Kuzuu, *J. Non-Cryst. Solids* **321**, 204 (2003).